PAPER • OPEN ACCESS

Ultrafast entanglement switching and singlet–triplet transitions control via structured terahertz pulses

To cite this article: Jonas Wätzel *et al* 2022 *New J. Phys.* **24** 043016

View the article online for updates and enhancements.

New Journal of Physics

The open access journal at the forefront of physics

PAPER

Ultrafast entanglement switching and singlet–triplet transitions control via structured terahertz pulses

Jonas Wätzel[1],[*] , Jamal Berakdar[1] and E Ya Sherman[2],[3]

[1] Institute for Physics, Martin-Luther-University Halle-Wittenberg, 06099 Halle, Germany
[2] Department of Physical Chemistry, University of the Basque Country UPV-EHU, 48940 Leioa, Spain
[3] IKERBASQUE, Basque Foundation for Science, Bilbao, Spain
[*] Author to whom any correspondence should be addressed.

E-mail: jonas.waetzel@physik.uni-halle.de

Abstract

Terahertz (THz) vector beams with spatially textured polarization are proposed to steer the spin and spatial distributions of two interacting electrons in a quantum dot. We study theoretically the spatiotemporal evolution of the spin and the charge-current densities and quantify the behavior of entanglement by calculating the concurrence. Both aspects are shown to be controllable efficiently and on the picosecond (ps) time scale by the parameters of the driving fields. Analyzing two different materials, GaAs and InGaAs, with different electron *g*-factors, we study the relationship between the *g*-factor and type of spin−orbit coupling required to produce efficient interlevel transitions. The results are useful for applications of quantum dots as basic nanoscale hardware elements in quantum information technology and for producing swiftly the appropriate spin and charge currents on demand.

1. Introduction

A key aspect in spintronics, a field [1–3] that utilizes spin dynamics for information processing and storage, is the role of the spin−orbit coupling (SOC), which opens the way to manipulate the spin state of charge carriers with electric fields. The spin manipulation by electric field, usually referred to as the electric dipole spin resonance (EDSR), was predicted by Rashba for bulk crystals [4] and observed in InSb [5, 6]. More recently, it was analyzed in details for two-dimensional electron gases in semiconductor heterostructures [7]. At low and moderate intensities of a propagating electromagnetic field, the electric field component drives the charge carriers' motion, and the spin is affected via SOC. Even at a relatively weak SOC, the impact of electric fields on the spin dynamics is more significant than the magnetic field component of the same wave. Growing interest in spin-dependent phenomena on the nanoscale led to the observation of the EDSR in GaAs quantum dots [8], and the subsequent theoretical analysis clarified the dot-specific features of the spin manipulation by the electric field [9–11]. The research has been mostly concentrated on various dynamical features of a single-electron motion caused by uniform monochromatic [12, 13], bichromatic [14], and pulse-shaped [15, 16] driving electric fields. For studying the role of spin-dependent electron−electron interaction and its potential for the use in quantum information, two-electron quantum dots have attracted considerable research (see, e.g. [17, 18]).

The energy scales corresponding to the orbital motion and the Coulomb interaction in nanosize two-dimensional semiconductor quantum dots entail the application of THz and sub-THz frequencies of external fields for inducing significant interlevel electron transitions. In addition to their energies, electromagnetic fields offer further parameters that affect the light–matter interactions. The present study highlights the potential of spatially structuring the polarization of the driving fields shaped as vector beams. We will be concerned with azimuthal vector beam (AVB) [19, 20] in which case the space-dependent polarization vector circulates around the optical axis. Vector beams can be produced by photoconductive antennas [21–24], mode conversion [25], velocity-mismatched optical rectification [26], and other means

[27, 28], and are of relevance in optoelectronic and optospintronic applications [29–32]. As shown here, AVB THz fields are an efficient tool for driving and shaping the spin dynamics in a two-electron quantum dot embedded in a semiconductor heterostructure.

The paper is organized as follows. Section 2 introduces the theoretical model and the main features of two-electron quantum dots and how vector beams interact with the dots. In section 3 we formulate the equations of motion for the corresponding density matrix and the observables of interest. These observables include the concurrence as a measure of entanglement and the spin and the charge densities. Numerical results for two materials (GaAs and InGaAs) will be presented in section 4, and the role of the electron g-factor and the symmetry of the SOC term (Rashba or Dresselhaus one) will be analyzed. Section 5 concludes the paper and the appendices contain additional analysis of the effect of the Coulomb interaction between the electrons.

2. Model: quantum dot in vector beam

2.1. Quantum dot

We consider a quantum dot with two active interacting electrons in a parabolic confinement. The Hamiltonian reads

$$\hat{H}_0 = \hat{H}_{\text{conf}} + \hat{H}_{\text{coul}} + \hat{H}_{\text{soc}} + \hat{H}_z, \tag{1}$$

where $\hat{H}_{\text{conf}}$ accounts for the kinetic energy and the single-particle confinement potential V

$$\hat{H}_{\text{conf}} = \sum_{i=1,2} \left(\frac{p_i^2}{2m^*} + V(\boldsymbol{r}_i) \right). \tag{2}$$

Here $\boldsymbol{r}_i = (x_i, y_i)$ is the position of the ith electron, m^* is the effective electron mass, and $\boldsymbol{p}_i = -i\hbar\partial_{\boldsymbol{r}_i} + eA(\boldsymbol{r}_i)$ is the kinetic momentum with e being the elementary charge and the speed of light $c = 1$. The vector potential $\boldsymbol{A}(x_i, y_i) = (-y_i, x_i)B_0/2$ generates a static magnetic field B_0 pointing in the z-direction. The potential reads $V(\boldsymbol{r}) = m^*\omega_0^2 r^2/2$. The electron–electron Coulomb interaction is given by (we use Gaussian units with $4\pi\epsilon_0 = 1$)

$$\hat{H}_{\text{coul}} = \frac{e^2}{\epsilon|\boldsymbol{r}_1 - \boldsymbol{r}_2|}, \tag{3}$$

where ϵ is the material-specific permittivity. The linear SOC is described by

$$\hat{H}_{\text{soc}} = \frac{1}{\hbar} \sum_{i=1,2} \left[\beta(p_y\sigma_y - p_x\sigma_x)_i + \alpha(p_x\sigma_y - p_y\sigma_x)_i \right], \tag{4}$$

where the sum runs over the particle index i and the σ_j ($j = x, y, z$) stand for the Pauli matrices. The SOC Hamiltonian $\hat{H}_{\text{soc}}$ contains two terms: the one proportional to β which originates from the bulk Dresselhaus SOC that is due to the absence of inversion symmetry in the GaAs lattice. The term proportional to α describes the Rashba SOC which can be present in quantum wells if the confining potential (in our case along the z-axis) is asymmetric. The Zeeman coupling due to the external magnetic field $\boldsymbol{B}$ is

$$\hat{H}_z = \frac{1}{2}g\mu_{\text{B}} \sum_{i=1,2} \boldsymbol{B} \cdot \boldsymbol{\sigma}_i, \tag{5}$$

where $\boldsymbol{\sigma}$ is the vector of Pauli matrices, g is the g-factor, and μ_{B} is the Bohr magneton.

In the spirit of the configuration interaction we obtain the two-electron spectrum in three steps. We first diagonalize the single electron Hamiltonian by using either numerical models or analytical methods. We do not consider the spin-dependent part (spin orbit, Zeeman) at this step. The single-particle eigen spectrum is known as the Fock–Darwin spectrum with the orbitals

$$\psi_{n,\ell}(r, \varphi) = C\rho^{|\ell|}e^{-\rho^2/2}L_n^{|\ell|}(\rho^2)e^{i\ell\varphi} \tag{6}$$

and energies

$$\varepsilon_{n,\ell} = \frac{\hbar^2}{m^* l_{\text{B}}^2}(2n + |\ell| + 1) + B_0\frac{e\hbar}{2m_{\text{e}}}\ell, \tag{7}$$

where $\rho = r/l_{\text{c}}$, and m_{e} is the free-electron mass. The confinement length is $l_{\text{c}} = (l_0^{-4} + l_{\text{B}}^{-4}/4)^{-1/4}$, where the 'harmonic oscillator' length is defined as $l_0 = \sqrt{\hbar/(m^*\omega_0)}$ and the 'magnetic length' is $l_{\text{B}} = \sqrt{\hbar/|e|B_0}$. The indices n and ℓ refer to the radial and angular quantum numbers, C is a normalization constant, and $L_{\text{p}}^\ell(x)$ are the associated Laguerre polynomials.

In the second step, using the single electron orbitals (6) the two-electron orbital Hamiltonian $\hat{H}_{\text{conf}} + \hat{H}_{\text{coul}}$ is diagonalized. The two-electron states are constructed to be symmetric

$$|\psi_s^{(\iota,\kappa)}\rangle = \frac{1}{\sqrt{2}}\left(|\psi_{\iota,1}\rangle|\psi_{\kappa,2}\rangle + |\psi_{\kappa,1}\rangle|\psi_{\iota,2}\rangle\right), \quad \iota \neq \kappa, \tag{8}$$

$$|\psi_s^{(\iota,k)}\rangle = |\psi_{\iota,1}\rangle|\psi_{\kappa,2}\rangle, \quad \iota = \kappa, \tag{9}$$

and antisymmetric

$$|\psi_{as}^{(\iota,\kappa)}\rangle = \frac{1}{\sqrt{2}}\left(|\psi_{\iota,1}\rangle|\psi_{\kappa,2}\rangle - |\psi_{\kappa,1}\rangle|\psi_{\iota,2}\rangle\right) \quad \iota \neq \kappa, \tag{10}$$

with respect to particle exchange. The index $\iota(\kappa)$ is a composite index for the unique single particle state with quantum numbers n and ℓ. The key quantities are the matrix elements

$$\langle\psi_a^{(\mu,\nu)}|\hat{H}_{\text{conf}} + \hat{H}_{\text{coul}}|\psi_b^{(\iota,\kappa)}\rangle = (\varepsilon_\iota + \varepsilon_\kappa)\delta_{\iota,\mu}\delta_{\kappa,\nu}\delta_{a,b} + \delta_{a,b}V_{ab}^{\mu,\nu,\iota,\kappa}, \tag{11}$$

where the indices a, b characterize the symmetry of the wave functions and

$$V_{ab}^{\mu,\nu,\iota,\kappa} = U_0 \int d^2r_1 \int d^2r_2 \frac{\left[\psi_a^{(\mu,\nu)}(\boldsymbol{r}_1,\boldsymbol{r}_2)\right]^* \psi_b^{(\iota,\kappa)}(\boldsymbol{r}_1,\boldsymbol{r}_2)}{|\boldsymbol{r}_1 - \boldsymbol{r}_2|}, \tag{12}$$

with $U_0 = e^2/\epsilon$. Depending on the participating states $|\psi_a^{\mu,\nu}\rangle$ and $|\psi_b^{\iota,\kappa}\rangle$ the matrix elements $V_{ab}^{\mu,\nu,\iota,\kappa}$ consist of two to four terms of the form

$$\mathcal{V}_{\mu,\nu,\iota,\kappa} = U_0 \int d^2r_1 \int d^2r_2 \frac{\psi_\mu^*(\boldsymbol{r}_1)\psi_\nu^*(\boldsymbol{r}_2)\psi_\iota(\boldsymbol{r}_1)\psi_\kappa(\boldsymbol{r}_2)}{|\boldsymbol{r}_1 - \boldsymbol{r}_2|}. \tag{13}$$

For the single particle orbitals (6), the analytical expressions for $\mathcal{V}_{\mu,\nu,\iota,\kappa}$ are given in the appendix A. The interacting two-electron orbitals $\phi_f(\boldsymbol{r}_1,\boldsymbol{r}_2)$ and energies ε_f (f is the two-particle index) are obtained via the diagonalization.

Finally, we account for the spin-dependent part of the total Hamiltonian $\hat{H}_0$. The orbital wave function ϕ_f is complemented by the spinor part $|\mathcal{S}\rangle \in \{S_0, T_0, T_+, T_-\}$, where $S_0 = (|\uparrow\downarrow\rangle - |\downarrow\uparrow\rangle)/\sqrt{2}$ is assigned to the singlet state whereas the spinor part of the triplet state reads $T_0 = (|\uparrow\downarrow\rangle + |\downarrow\uparrow\rangle)/\sqrt{2}$, $T_+ = |\uparrow\uparrow\rangle$, and $T_- = |\downarrow\downarrow\rangle$. The matrix elements of the total Hamiltonian $\hat{H}_0$ are

$$\langle\phi_f\mathcal{S}|\hat{H}_0|\phi_g\mathcal{S}'\rangle = \varepsilon_\alpha\delta_{f,g}\delta_{\mathcal{S},\mathcal{S}'} + g\mu_B B_0(\delta_{\mathcal{S},T_+} - \delta_{\mathcal{S}',T_-})\delta_{f,g}\delta_{\mathcal{S},\mathcal{S}'} + \sum_{i=1,2}\beta\langle\phi_f\mathcal{S}|(p_y\sigma_y - p_x\sigma_x)_i|\phi_g\mathcal{S}'\rangle$$

$$+ \sum_{i=1,2}\alpha\langle\phi_f\mathcal{S}|(p_x\sigma_y - p_y\sigma_x)_i|\phi_g\mathcal{S}'\rangle. \tag{14}$$

The sub-space matrix elements $\langle\mathcal{S}|\sigma_{x,i}|\mathcal{S}'\rangle$ and $\langle\mathcal{S}|\sigma_{y,i}|\mathcal{S}'\rangle$ can be worked out analytically exploiting $\langle\uparrow|\sigma_{x(y)}|\uparrow\rangle = \langle\downarrow|\sigma_{x(y)}|\downarrow\rangle = 0$. Finally, the matrix constructed from the elements $\langle\phi_f\mathcal{S}|\hat{H}_0|\phi_g\mathcal{S}'\rangle$ is diagonalized numerically to obtain the final eigenspectrum $\{|\Psi\rangle, E\}$. Thus, SOC is taken into account to all orders.

2.2. Azimuthal vector beam

The quantum dot is driven by an AVB with the vector potential [19, 29]

$$\boldsymbol{A}(\boldsymbol{r}, t) = A_0\frac{\rho}{w_0}e^{-\rho^2/w_0^2}\Omega(t)\cos(\omega t)\hat{\boldsymbol{e}}_\varphi, \tag{15}$$

fulfilling $\nabla \cdot \boldsymbol{A}(\boldsymbol{r}, t) = 0$. The beam with a donut-shaped intensity profile has the waist w_0. The temporal envelope is chosen as $\Omega(t) = \sin^2(\pi t/T_p)$ for $t \in [0, T_p]$ with the pulse duration being T_p and the carrier frequency ω. The azimuthal polarization vector is denoted by $\hat{\boldsymbol{e}}_\varphi$. Within the Poincaré gauge [29], the light-matter interaction reads

$$\hat{H}_{\text{int}}(t) = \frac{e}{m^*}\sum_{i=1,2}\boldsymbol{A}(\boldsymbol{r}_i)\cdot\hat{\boldsymbol{p}}_i + \frac{1}{\hbar}\sum_{i=1,2}\left[\alpha\left(A_x(t)\sigma_y - A_y(t)\sigma_x\right)_i + \beta\left(A_y(t)\sigma_y - A_x(t)\sigma_x\right)_i\right]$$

$$+ \frac{1}{2}g\mu_B\sum_{i=1,2}\tilde{\boldsymbol{B}}(\boldsymbol{r}_i, t)\cdot\boldsymbol{\sigma}_i. \tag{16}$$

The field acts as a strong magnetic pulse $\tilde{\boldsymbol{B}}(\boldsymbol{r},t) = \nabla \times \boldsymbol{A}(\boldsymbol{r},t)$ predominantly pointing in the z-direction [32]. The angular part of the vector potential can be cast in vector spherical harmonics [33] $\boldsymbol{\Phi}_{\ell,m} = \boldsymbol{r} \times \nabla Y_{\ell,m}$, where $Y_{\ell,m}$ are the spherical harmonics, leading to the expression for AVB vector potential

$$\boldsymbol{A}(\boldsymbol{r},t) = -A_0\sqrt{\frac{4\pi}{3}}f(\rho)g(t)\boldsymbol{\Phi}_{1,0}, \tag{17}$$

with $f(\rho) = (\rho/w_0)\exp(-\rho^2/w_0^2)$ and $g(t) = \Omega(t)\cos(\omega t)$. The angular representation is shown in figure 1(b). The orbital symmetry of the vector potential is clearly odd so that the interaction mediated by $\boldsymbol{A}(\boldsymbol{r}_i)\cdot\hat{\boldsymbol{p}}_i$ is even and no angular momentum is exchanged. Consequently, a light-induced transition between spin–orbit coupled states can be caused. For instance, in the considered two-electron quantum dot, $\hat{H}_{\mathrm{int}}$ mediates a transition between $|\Psi_1\rangle = |S_0\rangle + \alpha c_1|T_+\rangle$ and $|\Psi_2\rangle = |T_+\rangle + \alpha c_2|S_0\rangle$ (c_i are complex coefficients), which are coupled by Rashba SOC since for both $J_+ = 0$ [34]. Here, $J_\pm = \langle L_z\rangle \pm \langle \Sigma_z\rangle/2$, where the first (second) term is the expectation value of the state's total angular momentum (spin). Such transitions are specific to the AVB and are not possible with unstructured light pulses which lead to transitions characterized by odd multipoles (for example, dipole transitions).

As illustrated in figure 1(b) and evident from equation (15), the polarization direction of the field depends only on $\hat{\boldsymbol{e}}_\varphi$ and maintains its structure in the vicinity of the beam center. Thus, effects on the quantum dots related to the topology of the polarization do not depend on the waist (focusing) of the beam as long as the propagation axis pierces the dot center. In fact, if the beam is defocused on the scale of the quantum-dot size, quantum dots nearby the one we are interested in, experience effectively only a linearly polarized field. For a nanoscale stack of separated quantum dots, the transitions taking place in one dot are synchronized with same transitions in other dots.

3. Simulations: equation of motion and observables

3.1. Equation of motion

We are primarily interested in non-destructive (non-ionizing) ultrafast switching between spin-related states. Thus, the photon energy of the AVB is tuned to the resonant transition between the two lowest states, and the amplitude is kept low enough to ensure mainly one-photon processes. For the time evolution in the presence of the vector beam we solve numerically the von Neumann equation

$$i\hbar\frac{\partial\hat{\rho}}{\partial t} = \left[\hat{H}_0 + \hat{H}_{\mathrm{int}}(t),\hat{\rho}(t)\right]_- \tag{18}$$

using a Crank–Nicolson scheme [35]. The density operator is constructed from the final two-particle spectrum $\{|\Psi_k\rangle, E_k\}$, i.e., $\hat{\rho} = |\Psi\rangle\langle\Psi|$, and $[\ ]_-$ is the commutator. For simplicity, the initial state $\hat{\rho}_0$ is chosen as a fully occupied ground state for a fixed B_0. Hence, any relevant multi-photon transitions are captured by the numerical propagation of the density matrix. In principle, the approach allows the treatment of the coupling to various decay/decoherence channels which is not done in this short-time dynamics study.

3.2. Observables

As the observables we study the expectation value of the two-particle spin projection:

$$\langle\Sigma_z\rangle(t) = \mathrm{tr}\{\hat{\Sigma}_z\hat{\rho}(t)\}, \tag{19}$$

where $\hat{\Sigma}_z = \mathrm{diag}(2,0,0,-2)$. As a measure of the entanglement between the two electron spins we study the concurrence C which is calculated as [36]:

$$C(t) = \max(0,\lambda_1(t) - \lambda_2(t) - \lambda_3(t) - \lambda_4(t)), \tag{20}$$

where the $\lambda_i^2(t)$ are the eigenvalues of $R(t) = \hat{\rho}(t)\tilde{\rho}(t)$ in terms of the reduced density matrix of the two-electron spin states $\hat{\rho}_s(t)$ (obtained by tracing out the orbital part from $\hat{\rho}(t)$), and

$$\tilde{\rho}(t) = (\sigma_y \otimes \sigma_y)\hat{\rho}^*(t)(\sigma_y \otimes \sigma_y). \tag{21}$$

The time evolution of the electron charge density can be retrieved via $\rho(\boldsymbol{r},t) = \sum_{i=1,2}\rho_i(\boldsymbol{r},t)$, where

$$\rho_i(\boldsymbol{r}=\boldsymbol{r}_i,t) = \int \mathrm{d}^2r_j\,\rho_{2p}(\boldsymbol{r}_1,\boldsymbol{r}_2,t) \quad (j\neq i) \tag{22}$$

and $i, j = 1, 2$. The two-body density is

$$\rho_{2p}(\boldsymbol{r}_1, \boldsymbol{r}_2, t) = \text{tr} \left\{ |\boldsymbol{r}_1, \boldsymbol{r}_2\rangle\langle \boldsymbol{r}_1, \boldsymbol{r}_2| \hat{\rho}(t) \right\}. \tag{23}$$

Furthermore, we study

$$\rho_{\sigma, 2p}(\boldsymbol{r}_1, \boldsymbol{r}_2, t) = \text{tr} \left\{ |\boldsymbol{r}_1, \boldsymbol{r}_2\rangle\langle \boldsymbol{r}_1, \boldsymbol{r}_2| \hat{\sigma}_z \hat{\rho}(t) \right\}, \tag{24}$$

which we interpret as the time-dependent spin density.

We also introduce the two-particle spin-current density as the tensor operator [37]

$$\hat{j}_{\xi, \upsilon}^{s, 2p}(\boldsymbol{r}_1, \boldsymbol{r}_2) = \frac{1}{4} \sum_{i=1,2} \left[|\boldsymbol{r}_1, \boldsymbol{r}_2\rangle\langle \boldsymbol{r}_1, \boldsymbol{r}_2| (\hat{v}_\xi \hat{\sigma}_\upsilon)_i + (\hat{v}_\xi \hat{\sigma}_\upsilon)_i^\dagger |\boldsymbol{r}_1, \boldsymbol{r}_2\rangle\langle \boldsymbol{r}_1, \boldsymbol{r}_2| \right]. \tag{25}$$

The corresponding matrix elements read

$$\left[\hat{j}_{\xi, \upsilon}^{s, 2p}(\boldsymbol{r}_1, \boldsymbol{r}_2) \right]_{nm} = \frac{1}{4} \sum_{i=1,2} \left[\langle n|\boldsymbol{r}_1, \boldsymbol{r}_2\rangle\langle \boldsymbol{r}_1, \boldsymbol{r}_2| (\hat{v}_\xi \hat{\sigma}_\upsilon)_i|m\rangle + \langle n|(\hat{v}_\xi \hat{\sigma}_\upsilon)_i^\dagger |\boldsymbol{r}_1, \boldsymbol{r}_2\rangle\langle \boldsymbol{r}_1, \boldsymbol{r}_2|m\rangle \right]. \tag{26}$$

Here, we denote $\langle \boldsymbol{r}_1, \boldsymbol{r}_2|m\rangle \equiv \Psi_m(\boldsymbol{r}_1, \boldsymbol{r}_2)$. The index ξ indicates the spatial direction, and υ is the spin projection. The velocity operator is $\hat{\boldsymbol{v}} = (i/\hbar)[\hat{H}_0, \boldsymbol{r}]_-$. The expectation values of the spin-current operators are given by

$$j_{\xi, \upsilon}^{s, 2p}(\boldsymbol{r}_1, \boldsymbol{r}_2, t) = \text{tr} \left\{ \hat{j}_{\xi, \upsilon}^{s, 2p}(\boldsymbol{r}_1, \boldsymbol{r}_2, t) \hat{\rho}(t) \right\}. \tag{27}$$

Due to the symmetry of the laser field, it is instructive to investigate the spin-current densities in radial and azimuthal directions, i.e., we consider $\xi = r, \varphi$ in the cylindrical coordinates, together with the spin projection $\upsilon = z$. Similar to $\rho(\boldsymbol{r}, t)$ (see above), the measurable one-body spin-current density is then defined as $j_{\xi, \upsilon}^s(\boldsymbol{r}, t) = \sum_{i=1,2} \left[j_{\xi, \upsilon}^s(\boldsymbol{r}, t) \right]_i$, where

$$\left[j_{\xi, \upsilon}^s(\boldsymbol{r} = \boldsymbol{r}_i, t) \right]_i = \int \text{d}^2 r_p \, j_{\xi, \upsilon}^{s, 2p}(\boldsymbol{r}_1, \boldsymbol{r}_2, t) \quad (p \neq i), \tag{28}$$

with $i, p = 1, 2$.

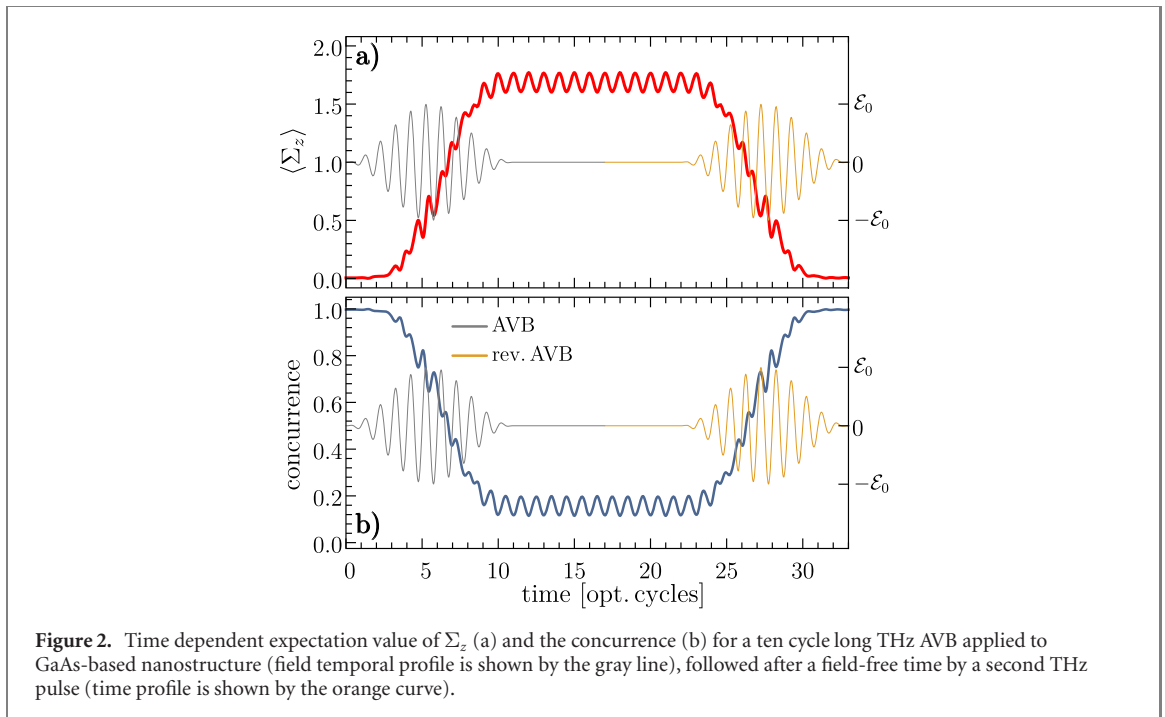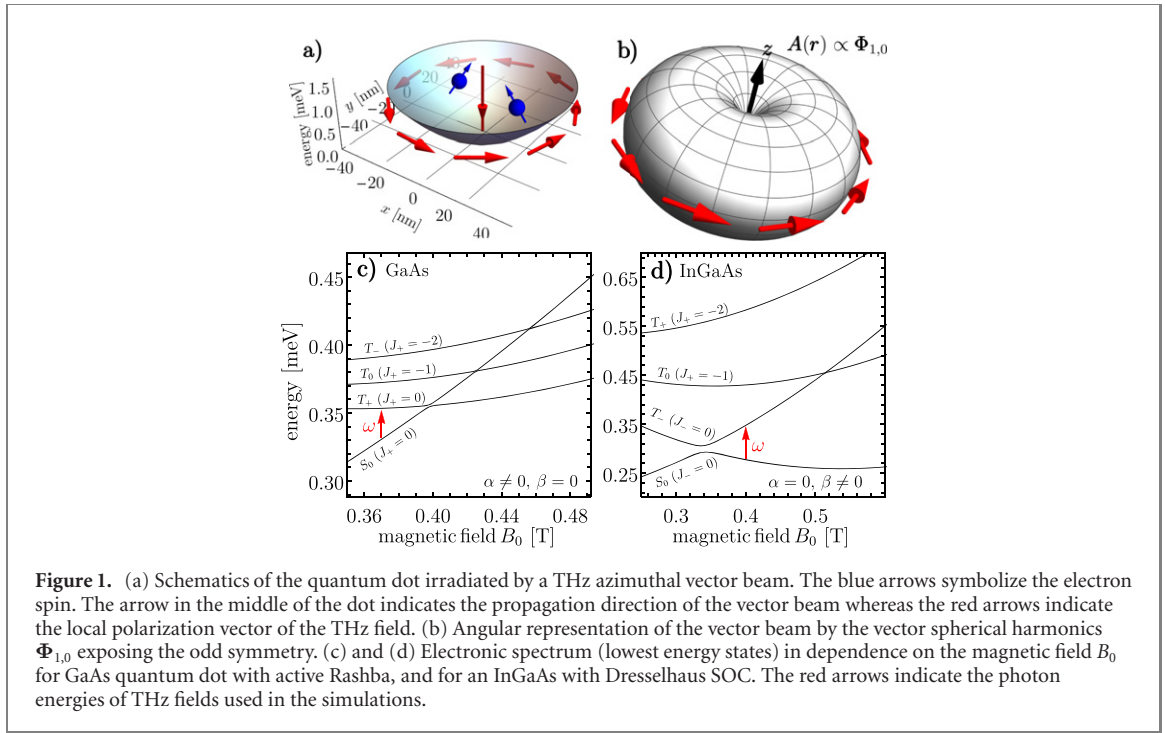## 4. Numerical results: the role of material

4.1. Electron states of GaAs and InGaAs quantum dots

We consider two different systems in our investigations. The first is a GaAs-based quantum dot with Rashba SOC with the parameters: the effective mass $m^* = 0.067 m_e$, the g-factor -0.44, $\epsilon = 12.9$, and a Rashba coefficient $\alpha = 5$ meV Å corresponding to an effective spin–orbit length $l_{so} \equiv \hbar^2/(m^* \alpha) = 1.26$ μm [38, 39]. The second investigated quantum dot structure is related to an inverted $\text{In}_{0.53}\text{Ga}_{0.47}\text{As}/\text{In}_{0.52}\text{Al}_{0.48}\text{As}$ heterostructure [40] with the parameters: $m^* = 0.054 m_e$, $g = 4$, $\epsilon = 14.2$ and the Dresselhaus coefficient $\beta = 5$ meV Å. To exclude the Rashba SOC, the quantum well (grown in the (001) direction) confinement along the z-direction is assumed to be symmetric [41]. In both cases we consider a harmonic oscillator interlevel distance of $\hbar\omega_0 = 1$ meV yielding the harmonic oscillator lengths $l_0 = \sqrt{\hbar/(m^* \omega_0)}$ of 32 nm and 37 nm for GaAs and InGaAs, respectively. From a technical point of view, for convergence of the whole diagonalization 50 single-particle states were needed. The pulse duration is set to 10 field cycles.

Figures 1(c) and (d) show the energies of the four lowest eigen states for different values of the magnetic field strength B_0. Considering transitions at $B_0 \approx 0.4$ T, where $l_B \approx 40$ nm, then $l_c \approx l_0$ and the corresponding Coulomb interaction energy $e^2/(\epsilon l_0) \approx 3$ meV, indicating the essential effect of the Coulomb interactions. Depending on the SOC type, crossing and anti-crossing occur for energy states as we scan the magnetic field strength. Generally, for $B_0 \to 0$, the ground state is the singlet state S_0 while the branch of triplet states are separated by the Zeeman splitting energy $\sim g\mu_B B_0$. For a GaAs-type quantum dot (the g-factor is negative), we find a small-gap anti-crossing between S_0 and T_+ [34] due to the active Rashba SOC interaction, which conserves J_+. In contrast, for the InGaAs-type quantum dot, $g > 0$ and Dresselhaus SOC interaction is active. It conserves J_- so that we find again an anti-crossing between the two lowest states.

4.2. Entanglement dynamics and singlet–triplet transitions in a GaAs quantum dot
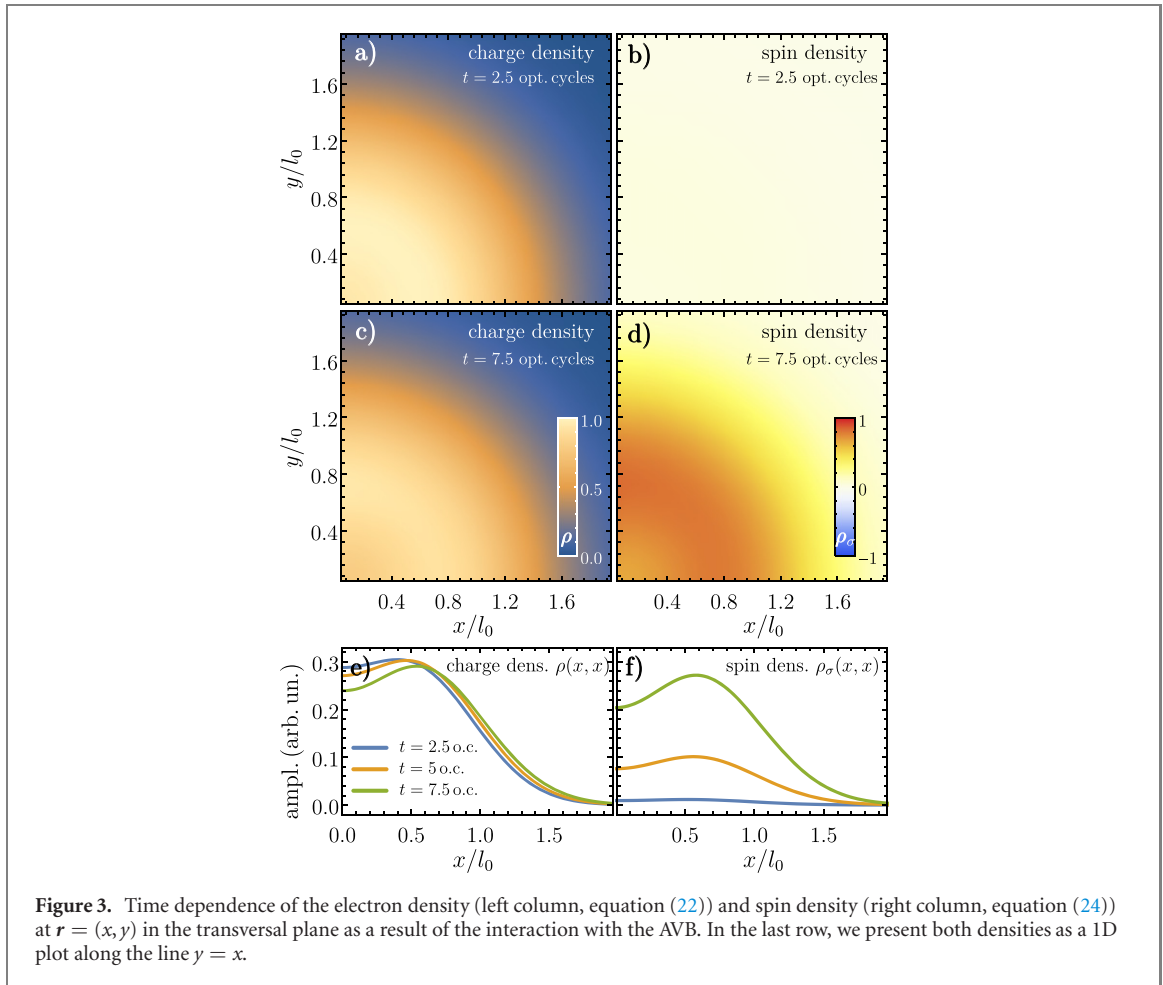
The pulse carrier frequency ω is chosen to be resonant with the transition between the two lowest energy states, i.e., $\hbar\omega = E_2 - E_1$, at $B_0 = 0.37$ T which means just below the S–T anti-crossing that is indicated by

Figure 1. (a) Schematics of the quantum dot irradiated by a THz azimuthal vector beam. The blue arrows symbolize the electron spin. The arrow in the middle of the dot indicates the propagation direction of the vector beam whereas the red arrows indicate the local polarization vector of the THz field. (b) Angular representation of the vector beam by the vector spherical harmonics $\Phi_{1,0}$ exposing the odd symmetry. (c) and (d) Electronic spectrum (lowest energy states) in dependence on the magnetic field B_0 for GaAs quantum dot with active Rashba, and for an InGaAs with Dresselhaus SOC. The red arrows indicate the photon energies of THz fields used in the simulations.

Figure 2. Time dependent expectation value of Σ_z (a) and the concurrence (b) for a ten cycle long THz AVB applied to GaAs-based nanostructure (field temporal profile is shown by the gray line), followed after a field-free time by a second THz pulse (time profile is shown by the orange curve).

the red arrow in figure 1. For a sizable transition probability the pulse electric field strength is chosen as 112 kV cm^{-1} at the peak intensity (the beam waist is around 0.1 mm) which yields $\mathcal{E} = 190$ V cm^{-1} at $l_0 = 32$ nm. Such strong sub-THz fields are feasible with current techniques [42]. The interaction with an AVB conserves angular momentum so that in the absence of any SOC the laser field would not initiate a transition between the lowest states. As clear from equation (16), the Rashba SOC enables the pulse to drive transition between the singlet and triplet states, as quantified in figure 2.

We remark that the proposed scheme for triggering spin transitions between the lowest states would not work with circularly polarized field, since an angular momentum exchange of one $\hbar$ is implied. Considering the transition scheme in figure 1(c), no coupling between singlet S_0 and triplet state T_+ is thus possible since J_z is not conserved when applying a circular laser field.

Pulse-driving the population from the ground to the triplet state increases the spin projection $\langle \Sigma_z \rangle$ to a value close to two, indicating that both electron spins states are roughly aligned. We note that the results are

Figure 3. Time dependence of the electron density (left column, equation (22)) and spin density (right column, equation (24)) at $\boldsymbol{r} = (x, y)$ in the transversal plane as a result of the interaction with the AVB. In the last row, we present both densities as a 1D plot along the line $y = x$.
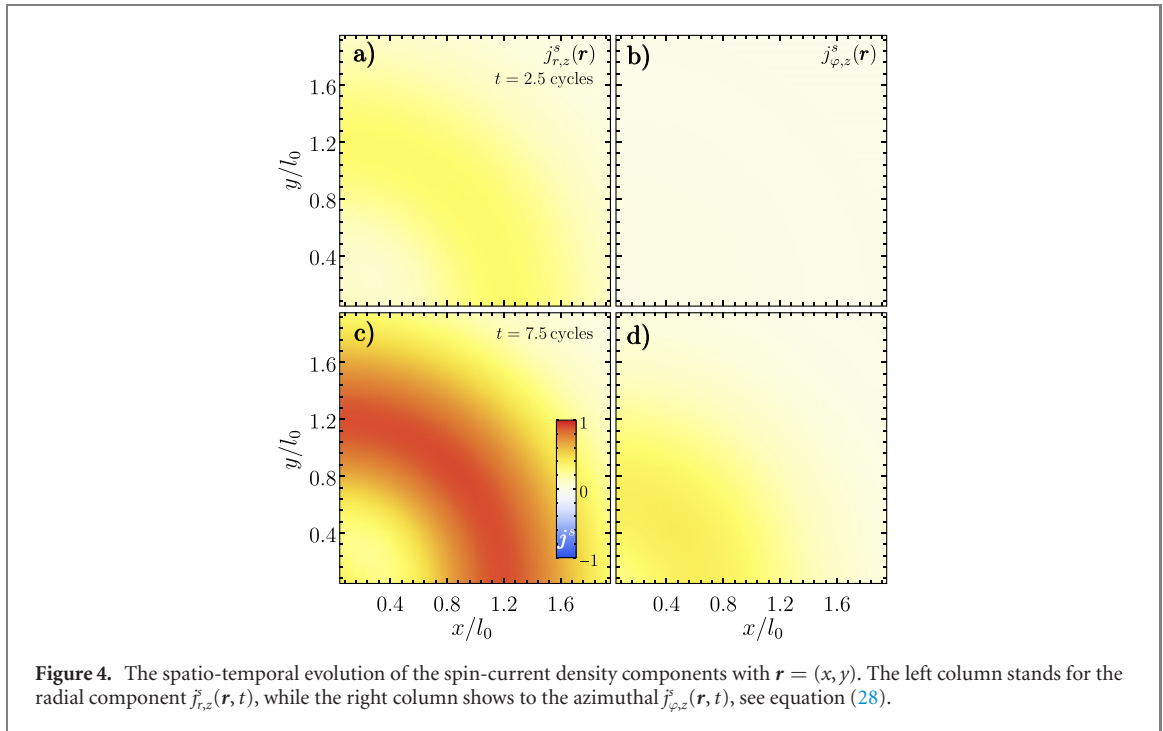
obtained by full numerical simulations beyond the rotating wave approximation and that $[\hat{H}_0, \Sigma_z]_- \neq 0$ leading to the relatively fast oscillations during the population transfer. The Fourier transform of the field-free oscillations between the AVB pulses reveals the dominating frequency $\omega \cong 3 \times 10^{12}$ s^{-1} matching the energy difference between singlet and triplet states. Consequently, the oscillations originate from small-amplitude probability transitions between these states. In addition, a complete population inversion is not achieved, and hence $\langle \Sigma_z \rangle$ does not reach the maximal value of two. The analysis of the contributions of different terms in equation (16) reveals that $\boldsymbol{A} \cdot \hat{\boldsymbol{p}}$ has the most pronounced impact on the transition. The Zeeman term produced by the AVB magnetic field $\tilde{\boldsymbol{B}}(\boldsymbol{r}, t)$ results in a relative correction to the transition probability which is respectively less then 1% or 5% in GaAs or InGaAs structures.

For the behavior of entanglement expressed by C we expect the inverse behavior of $\langle \Sigma_z \rangle$. The singlet state S_0 from which we start is a maximally entangled (Bell) state. The triplet state T_+ is expressible as a product state. Figure 2(b) evidences the possibility of a full temporal control of transitions between the entangled and non-entangled states by applying sequential pulses. For instance, by applying a *reversed* AVB pulse propagating in the $-z$-direction so that $\boldsymbol{A}_{\text{rev}}(\boldsymbol{r}, t) = -\boldsymbol{A}(\boldsymbol{r}, t - t_2)$ in the $z = 0$ plane (cf equation (15), t_2 is the application time of the reversed AVB), we can elegantly reverse the spin polarization. We note that experimentally, those initial and reversed pulses can be realized in the geometry of a 'vertical' quantum dot located on a thin substrate extended in the zy-plane with the initial and reversed AVB propagating in the $-x$ and x-directions, respectively.

The spatial resolution is set by the size of the quantum dot and not by the waist of the pulse. Thus, in our case the resolution is way below the diffraction limit. Other quantum dots separated from our quantum dot by a fraction of the pulse waist experience a marginal S–T transition since the local pulse is almost homogeneously linearly polarized. To endorse this statement we provide an example in the appendix D, where the time-dependent $\langle \Sigma_z \rangle$ of a quantum dot located at a distance of $\lambda/4$, where λ is the laser wavelength, relative to the optical axis shows no sizable S–T transition.

Figure 2 shows integrated quantities regarding spin polarization and entanglement. Differential information are obtained by following the dynamics of the charge and spin densities. We start analyzing the single particle charge and spin densities $\rho(\boldsymbol{r}, t)$ and $\rho_\sigma(\boldsymbol{r}, t)$, which are shown in figure 3. For illustrations, snapshots are taken at the time of application of the AVB ($t = 2.5$ field cycles) and at the end of the

Figure 4. The spatio-temporal evolution of the spin-current density components with $r = (x, y)$. The left column stands for the radial component $j^s_{r,z}(r, t)$, while the right column shows to the azimuthal $j^s_{\varphi,z}(r, t)$, see equation (28).
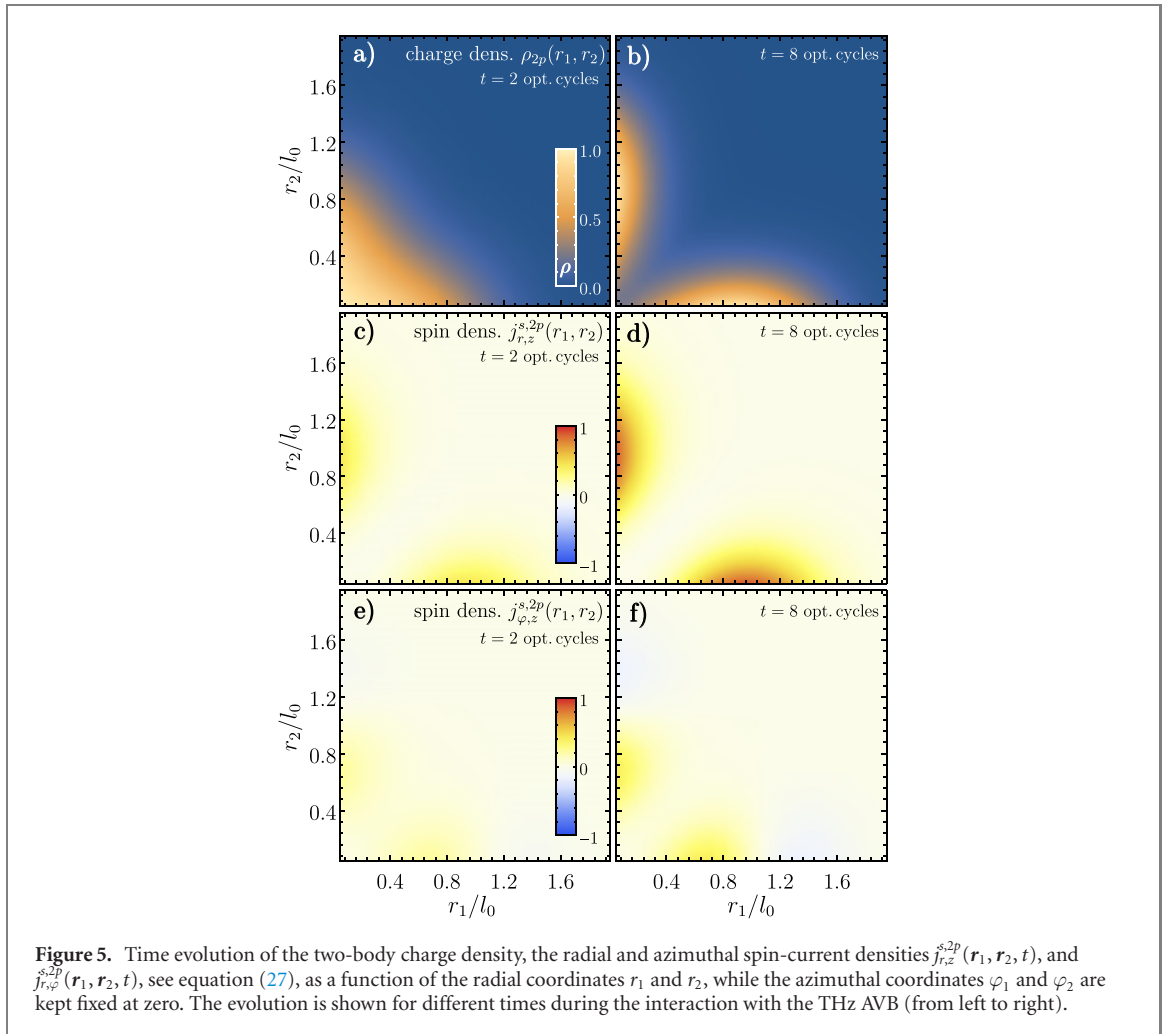
interaction with the pulse ($t = 7.5$ cycles). The basic shape of the initial charge density is inferred from the shape of the wave function, as given by equation (6) (additional effects such as electron–electron interaction are discussed below). Figures 3(a) and (c) confirm our expectation that the AVB does not affect substantially the orbital motion. For the case shown in figure 3, the electron–electron interaction has a minor influence pushing slightly the density to outer radii, as observed in figure 3(e). Larger effects of the AVB pulse are expected for the spin density: starting from the singlet-state, the AVB pulse effectively spin polarizes the quantum dots by populating the triplet state. Figures 3(d) and (f) evidence that at the end of the light–matter interaction, the quantum dot is nearly fully spin-polarized.

The AVB effectively spin-polarizes the quantum dot indicating a flow of spin-angular momentum, which is reflected in the behavior of the spin-current density. Figure 4 shows the time and spatial dependencies of the spin-current densities in the orbital radial and azimuthal directions. Both the quantum dot and the AVB are cylindrical symmetric around the beam axis and so is the spin-current density. The fact that the dot is spin-polarized after the pulse implies that the spin-current density is propagating in radial direction, as emphasized by figure 4. The radial structure in figure 4(c) can be understood from the behavior of the velocity operator and the charge density shown in figure 3(d). The AVB leads to angular oscillations around the beam axis of the almost rigid charge density. Thus, the charge distribution is hardly changing but the angular momentum and hence, the angular velocity oscillates transiently with zero time average. Therefore, during the dynamics the radial velocity increases with the radial distance which, when combined with figure 3(d), leads to the radial behavior in figure 4(c) of the spin-current density.

More details are expected for the two-particle quantities. In general, we expect that the electron–electron interaction suppresses the density when the electrons approach each others. In addition, the orbital part of the triplet state is antisymmetric with respect to the particle exchange, and hence the density diminishes in this case when the two particles are at the same position (both effects lead to the exchange and correlation hole). This scenario is basically confirmed by figure 5 which shows the evolution of the two-body densities $\rho_{2p}(r_1, r_2, t), j^{s,2p}_{r,z}(r_1, r_2, t)$, and $j^{s,2p}_{\varphi,z}(r_1, r_2, t)$ in the ground state and at the end of interaction with the vector beam. We observe a local minimum formed at the line $r_1 = r_2$ while the interaction with the AVB pumps the population into the triplet state. The change in the density results in the emergence of the radial spin-current density, as revealed by the split high intense structures in figure 5(d). The pronounced minimum in the density at $r_1 = r_2$ starts to disappear when increasing the Rashba SOC strength due to the enhanced mixing between the different spin states.

4.3. Vector-beam-driven T–S transitions in an InGaAs quantum dot

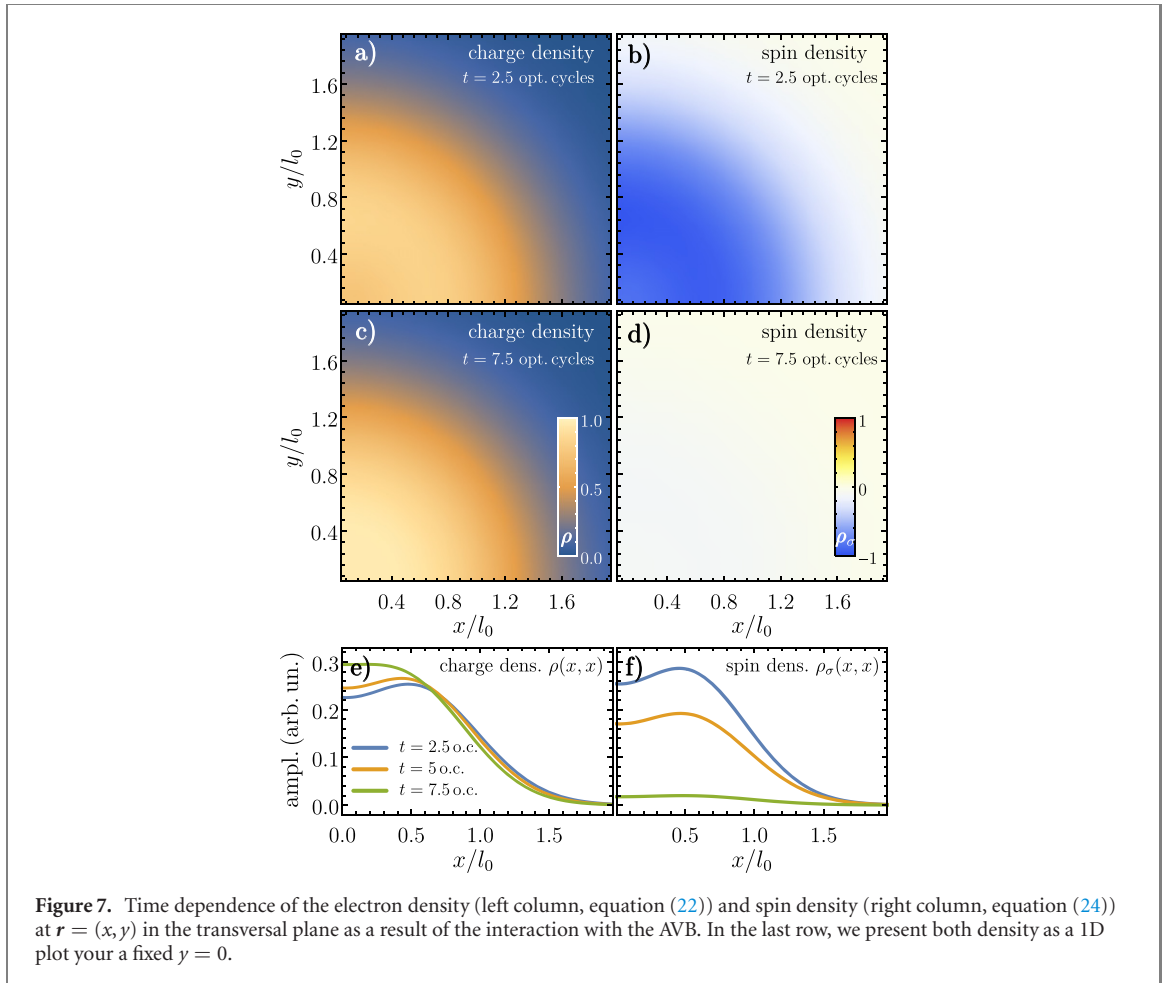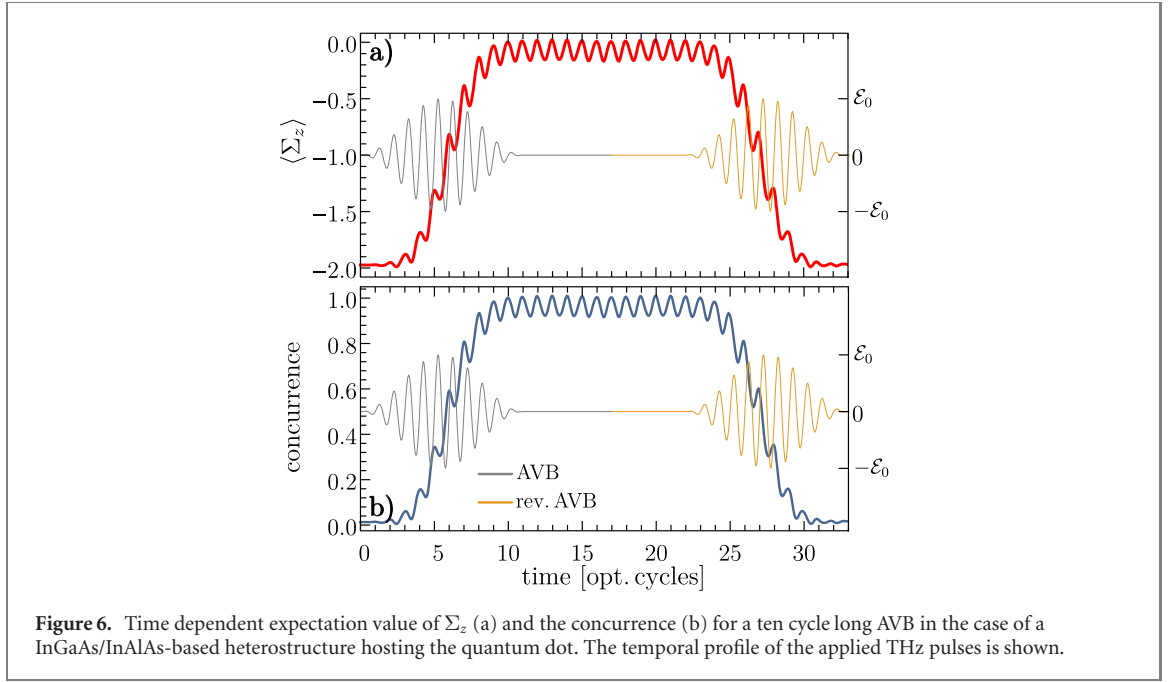As indicated in figure 1(d), for InGaAs the magnetic field B_0 is such that we are beyond the Dresselhaus-induced anti-crossing point and the triplet is the ground state. Due to the positive *g*-factor, T_+ and T_- exchange their roles, in comparison to GaAs, meaning that singlet and triplet can only be coupled in the presence of Dresselhaus coupling, which conserves J_- (zero for S_0 and T_-).

Figure 5. Time evolution of the two-body charge density, the radial and azimuthal spin-current densities $j^{s,2p}_{r,z}(\boldsymbol{r}_1,\boldsymbol{r}_2,t)$, and $j^{s,2p}_{r,\varphi}(\boldsymbol{r}_1,\boldsymbol{r}_2,t)$, see equation (27), as a function of the radial coordinates r_1 and r_2, while the azimuthal coordinates φ_1 and φ_2 are kept fixed at zero. The evolution is shown for different times during the interaction with the THz AVB (from left to right).

As the vector beam conserves angular momentum, a laser-driven T−S transition relies on active SOC. In figure 6, we present the expectation value of Σ_z and the corresponding entanglement measure C. One may view the whole process as a reversed one to the GaAs case. By initiating the T−S transition with the AVB pulse, we drive the spin projection expectation value $\langle\Sigma_z\rangle$ to zero, in other words from quasi-alignment (of the individual electron spins) to high degree anti-alignment. This is reflected in the behavior of the concurrence shown in figure 6(b), which is virtually zero in the ground state and rises to nearly unity (high degree of entanglement) during the interaction. Again, since $[\hat{H}_0,\hat{\Sigma}_z]_- \neq 0$ and $[\hat{H}_0,C]_- \neq 0$ the time oscillations of both quantities continue after the THz field is switched off. As before, we have full control over the entanglement: by applying a second RVB propagating in the opposite direction (the time profile is indicated by the yellow dashed line), we reverse the T−S transition which means we decrease the concurrence.
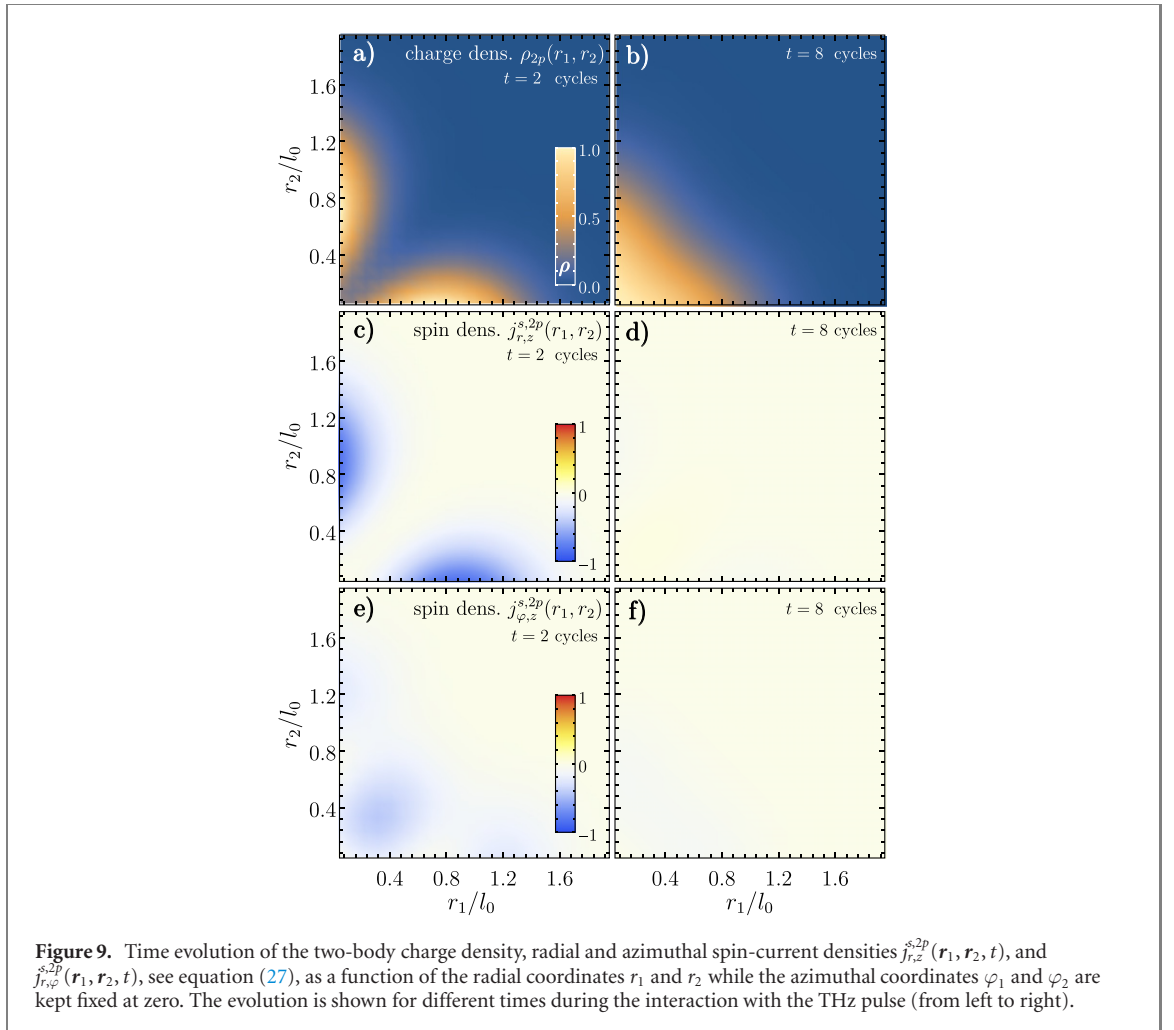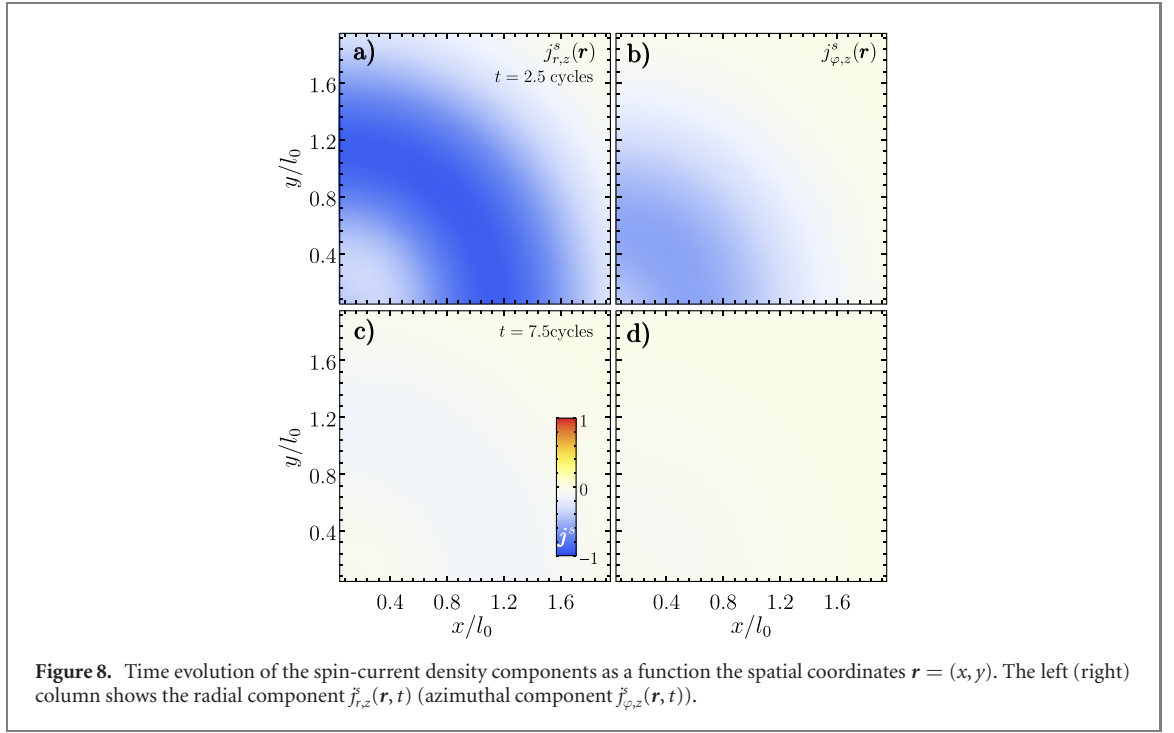
In figure 7, we present the evolution of the spatially resolved total charge and spin densities, which can be interpreted as the reversed processes presented in figure 3. In the ground state, the spin density is nearly fully polarized, as indicated by the blue structure in figures 7(b) and (f). In contrast to the GaAs, where we considered population transfer to T_+, the initial spin polarization of the density reflects strongly the spin state of the ground state T_-. The vector beam enables a nearly complete depolarization of the spin density, as presented by figure 7(d) corresponding to a time at the end of the interaction. It evidences an effective T−S transition and population transfer. Overall, the interaction of the AVB does not change the general structure of the density as no orbital angular momentum is exchanged. This underlines our interpretation that the AVB acts in principle as a short magnetic pulse, whereas the field is cylindrically symmetric and points predominantly in the z-direction.

The time evolution of the corresponding spin current density is shown in figure 8. Due to the strong static magnetic field ($B_0 = 0.4$ T), we find intrinsic spin currents in the ground state, as indicated by panel (a). While the radial component exhibits a negative spin-current density, reflected in the sign of the spin density and the alignment of the electron spins in the ground state, we also find a weak azimuthal component. Both reveal a radial symmetry similar to the charge and spin densities. In the GaAs case we discussed above, we injected spin currents by the light–matter interaction. Here, we achieve the reversed

Figure 6. Time dependent expectation value of Σ_z (a) and the concurrence (b) for a ten cycle long AVB in the case of a InGaAs/InAlAs-based heterostructure hosting the quantum dot. The temporal profile of the applied THz pulses is shown.

Figure 7. Time dependence of the electron density (left column, equation (22)) and spin density (right column, equation (24)) at $\boldsymbol{r} = (x, y)$ in the transversal plane as a result of the interaction with the AVB. In the last row, we present both density as a 1D plot your a fixed $y = 0$.

process, i.e., we are able to break down the spin currents as seen from the results shown in the second row of figure 8. We effectively reduce the magnitude of both spatial components which we attribute to the population transfer, i.e., a quasi complete T–S transition driven by the AVB.

Figure 9 shows the two-body densities $\rho(\boldsymbol{r}_1, \boldsymbol{r}_2)$, $j^s_{r,z}(\boldsymbol{r}_1, \boldsymbol{r}_2)$, and $j^s_{\varphi,z}(\boldsymbol{r}_1, \boldsymbol{r}_2)$ as functions of r_1 and r_2 at the angles $\varphi_1 = \varphi_2 = 0$ for a time at the beginning and at the end of the AVB-quantum dot interaction. As the ground state is the triplet, we find the symmetrical 'density splits' at $r_1 = r_2$ for $t \to 0$ as well as a symmetry

Figure 8. Time evolution of the spin-current density components as a function the spatial coordinates $\boldsymbol{r} = (x,y)$. The left (right) column shows the radial component $\breve{j}^s_{r,z}(\boldsymbol{r},t)$ (azimuthal component $\breve{j}^s_{\varphi,z}(\boldsymbol{r},t)$).

Figure 9. Time evolution of the two-body charge density, radial and azimuthal spin-current densities $j^{s,2p}_{r,z}(\boldsymbol{r}_1,\boldsymbol{r}_2,t)$, and $j^{s,2p}_{r,\varphi}(\boldsymbol{r}_1,\boldsymbol{r}_2,t)$, see equation (27), as a function of the radial coordinates r_1 and r_2 while the azimuthal coordinates φ_1 and φ_2 are kept fixed at zero. The evolution is shown for different times during the interaction with the THz pulse (from left to right).

with respect to this line. Note that in comparison to the S–T transitions GaAs-based dot the minimum along $r_1 = r_2$ is much more pronounced. During the interaction with the AVB the gap in the charge density

related $\rho(\boldsymbol{r}_1, \boldsymbol{r}_2)$ starts to close and the whole density becomes more and more homogeneous, which can be explained by the population transfer into the singlet state. The results show that a nearly complete occupation of the singlet is possible by driving the quantum dot with the AVB. The change in the charge density reflects the disappearing of the radial current density component as the magnitude of the nodal structures decreases drastically during the interaction.

5. Conclusions

We studied the spin and orbital steering of the quantum states in an interacting two-electron quantum dot utilizing THz AVBs. Performing full quantum dynamic simulations for GaAs and InGaAs-based dots, we conclude that the total electron spin is controllable by an appropriate field-driving of singlet–triplet transitions. We analyzed the vector-beam driven spin and charge currents and identified them as the underlying source for the patterns observed in the spatio-temporal evolution of the total spin and in the concurrence. By comparing GaAs and InGaAs we demonstrated the importance of the *g*-factor and the type of SOC. The results point to a new route for controlling the charge and spin dynamics in interacting quantum dots by applying currently available polarization textured THz fields.

Acknowledgments

Data availability statement

The data that support the findings of this study are available upon reasonable request from the authors.
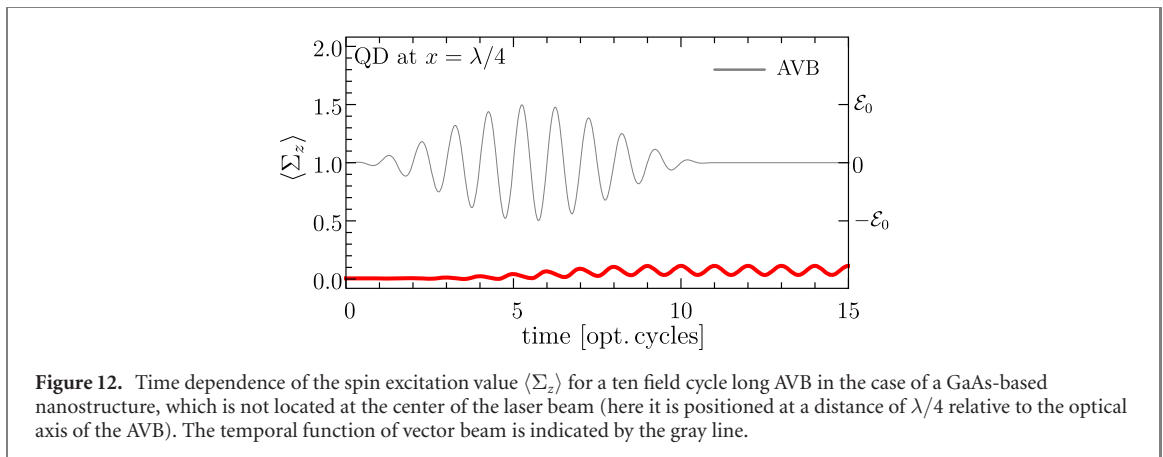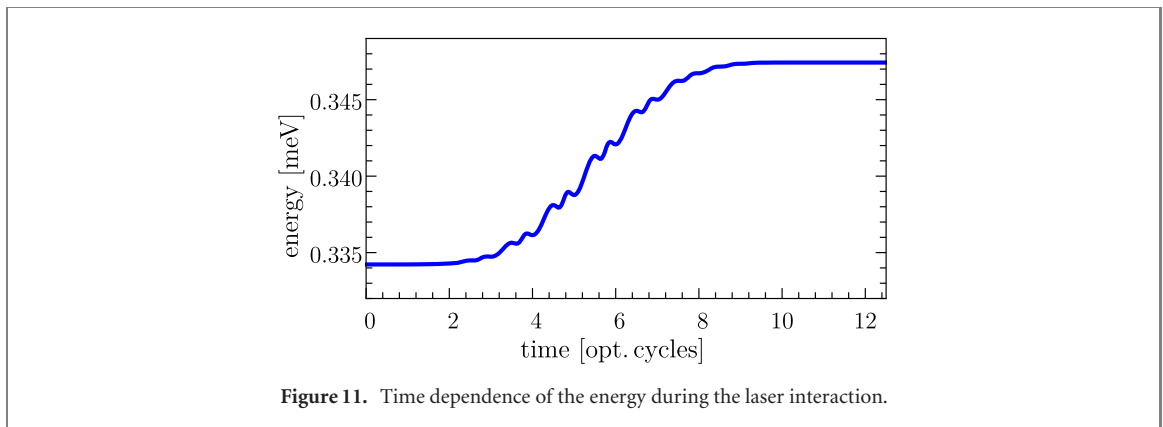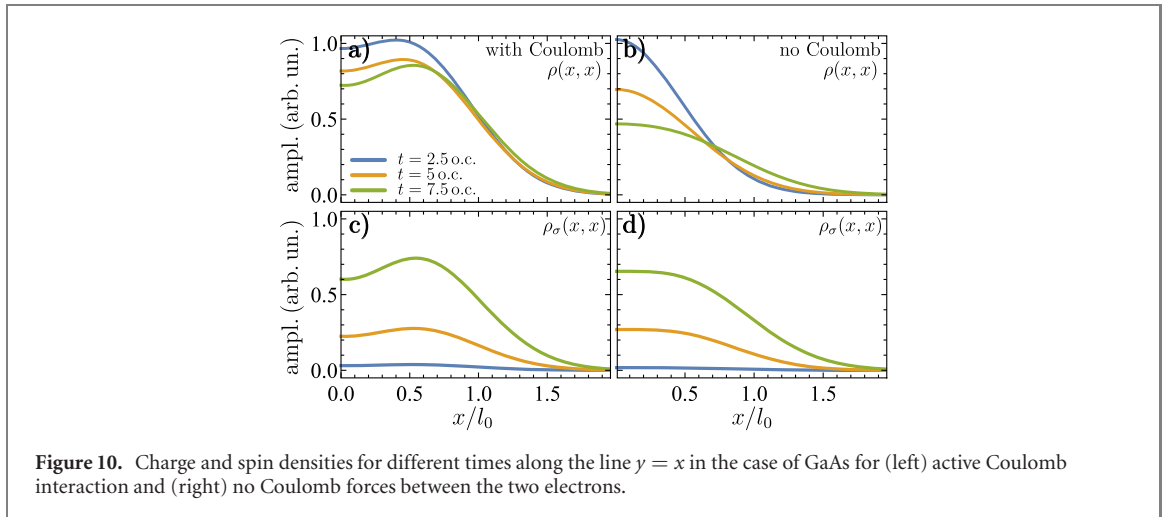
Appendix A. Coulomb matrix elements

In the case of a parabolic confinement potential with the corresponding 'harmonic oscillator' length l_0, the Coulomb matrix elements can be expressed as [43–45]

$$
\begin{aligned}
\mathcal{V}_{1,2,3,4} &= \frac{U_0}{l_0} \int \mathrm{d}^2 q_1 \int \mathrm{d}^2 q_2 \frac{\psi_1^*(\boldsymbol{q}_1)\psi_2^*(\boldsymbol{q}_2)\psi_3(\boldsymbol{q}_1)\psi_4(\boldsymbol{q}_2)}{|\boldsymbol{q}_1 - \boldsymbol{q}_2|} \\
&= \frac{U_0}{l_0}\delta_{\ell_1+\ell_2,\ell_3+\ell_4} \frac{(-1)^\phi}{\sqrt{\mu_1!\nu_1!\mu_2!\nu_2!\mu_3!\nu_3!\mu_4!\nu_4!}} \sum_{s_1=0}^{\min(\mu_1,\mu_3)} s_1! \binom{\mu_1}{s_1}\binom{\mu_3}{s_1} \sum_{s_2=0}^{\min(\mu_2,\mu_4)} s_2! \binom{\mu_2}{s_2}\binom{\mu_4}{s_2} \\
&\quad \times \sum_{s_3=0}^{\min(\nu_1,\nu_3)} s_3! \binom{\nu_1}{s_3}\binom{\nu_3}{s_3} \sum_{s_4=0}^{\min(\nu_2,\nu_4)} s_4! \binom{\nu_2}{s_4}\binom{\nu_4}{s_4} \frac{(-1)^s\Gamma\left(s+1/2\right)}{2^{s+1/2}},
\end{aligned} \tag{A1}
$$

where $\boldsymbol{q}_i = \boldsymbol{r}_i/l_0$ ($i = 1, 2$) and the prefactor determines the energy scale of the Coulomb potential in terms of l_0. The expression involves the representation by two integers $\mu_k = n_k + (|\ell_k| + \ell_k)/2$ and $\nu_k = n_k + (|\ell_k| - \ell_k)/2$ associated with ladder operators in Fock space. Further, we define $s = \mu_1 + \mu_2 + \nu_3 + \nu_4 - (s_1 + s_2 + s_3 + s_4)$ and $\phi = \max(\mu_1, \nu_1) + \min(\mu_2, \nu_2) + \max(\mu_3, \nu_3) + \min(\mu_4, \nu_4)$. The conservation of the total angular momentum by Coulomb interaction is implied here.

Appendix B. Effect of Coulomb interaction

In figure 10, we briefly discuss the impact of the Coulomb interaction on the time evolution of the charge and spin densities for GaAs. Switching off the Coulomb forces between the two electrons, the density increases considerably in size during the population transfer. Figure 10 indicates that despite the relatively large dot size (confinement length $l_0 = 32$ nm), the long-range Coulomb interaction is important.

Figure 10. Charge and spin densities for different times along the line $y = x$ in the case of GaAs for (left) active Coulomb interaction and (right) no Coulomb forces between the two electrons.

Figure 11. Time dependence of the energy during the laser interaction.

Figure 12. Time dependence of the spin excitation value $\langle \Sigma_z \rangle$ for a ten field cycle long AVB in the case of a GaAs-based nanostructure, which is not located at the center of the laser beam (here it is positioned at a distance of $\lambda/4$ relative to the optical axis of the AVB). The temporal function of vector beam is indicated by the gray line.

Appendix C. Time-dependent energy

Our control scheme is not only efficient in that a high degree of polarization and strong concurrence are achieved by the THz pulses but also non-invasive and energy-efficient. One indication is shown in figure 11 which shows the energy evolution of the GaAs quantum dot during the interaction with THz field. No substantial high energy excitations are caused.

Appendix D. Nanoscale resolution and off-axis quantum dot excitation

We assume that we are able to control the quantum dot spin polarization on a length scale below the diffraction limit. To support this statement, we shift the THz beam by $\lambda/4$ (with λ is the THz wavelength)

away from the quantum dot and monitor the spin polarization in a GaAs quantum dot. The result shown in figure 12 is a clearly reduced spin polarization due to the fact that at the location of the quantum dot the THz field can be viewed as linearly polarized.

ORCID iDs

Jonas Wätzel ⓘ https://orcid.org/0000-0001-8817-0933
Jamal Berakdar ⓘ https://orcid.org/0000-0001-8727-3981

References

[1] Wolf S A, Awschalom D D, Buhrman R A, Daughton J M, von Molnaír S, Roukes M L, Chtchelkanova A Y and Treger D M 2001 *Science* **294** 1488
[2] Žutić I, Fabian J and Sarma S 2004 *Rev. Mod. Phys.* **76** 323
[3] Bader S D and Parkin S S P 2010 *Annu. Rev. Condens. Matter Phys.* **1** 71
[4] Rashba E I 1960 *Sov. Phys. Solid State* **2** 1109
[5] Bemski G 1960 *Phys. Rev. Lett.* **4** 62
[6] Bell R L 1962 *Phys. Rev. Lett.* **9** 52
[7] Rashba E I and Efros A L 2003 *Phys. Rev. Lett.* **91** 126405
[8] Nowack K C, Koppens F H L, Nazarov Y V and Vandersypen L M K 2007 *Science* **318** 1430
[9] Golovach V N, Borhani M and Loss D 2006 *Phys. Rev.* B **74** 165319
[10] Jiang J H, Weng M Q and Wu M W 2006 *J. Appl. Phys.* **100** 063709
[11] Khomitsky D V, Gulyaev L V and Sherman E Y 2012 *Phys. Rev.* B **85** 125312
[12] Romhányi J, Burkard G and Pályi A 2015 *Phys. Rev.* B **92** 054422
[13] Khomitsky D, Lavrukhina E and Sherman E Y 2020 *Phys. Rev. Appl.* **14** 014090
[14] Najmaie A, Sherman E Y and Sipe J E 2005 *Phys. Rev. Lett.* **95** 056601
[15] Ban Y, Chen X, Sherman E Y and Muga J G 2012 *Phys. Rev. Lett.* **109** 206602
[16] Veszeli M T and Pályi A 2018 *Phys. Rev.* B **97** 235433
[17] Creffield C E and Platero G 2002 *Phys. Rev.* B **65** 113304
[18] Nishi Y, Tokura Y, Gupta J, Austing G and Tarucha S 2007 *Phys. Rev.* B **75** 121301
[19] Zhan Q 2009 *Adv. Opt. Photon.* **1** 1
[20] Veysi M, Guclu C and Capolino F 2015 *J. Opt. Soc. Am.* B **32** 345
[21] Deibel J A, Wang K, Escarra M D and Mittleman D 2006 *Opt. Express* **14** 279
[22] Winnerl S, Zimmermann B, Peter F, Schneider H and Helm M 2009 *Opt. Express* **17** 1571
[23] Winnerl S, Hubrich R, Mittendorff M, Schneider H and Helm M 2012 *New J. Phys.* **14** 103049
[24] Cliffe M J, Rodak A, Graham D M and Jamison S P 2014 *Appl. Phys. Lett.* **105** 191112
[25] Grosjean T *et al* 2008 *Opt. Express* **16** 18895
[26] Chang G, Divin C J, Liu C-H, Williamson S L, Galvanauskas A and Norris T B 2007 *Opt. Lett.* **32** 433
[27] Minami Y, Kurihara T, Yamaguchi K, Nakajima M and Suemoto T 2013 *Appl. Phys. Lett.* **102** 151106
[28] Zheng Z, Kanda N, Konishi K and Kuwata-Gonokami M 2013 *Opt. Express* **21** 10642
[29] Wätzel J, Granados-Castro C M and Berakdar J 2019 *Phys. Rev.* B **99** 085425
[30] Wätzel J and Berakdar J 2016 *Sci. Rep.* **6** 21475
[31] Wätzel J and Berakdar J 2018 *Sci. Rep.* **8** 17102
[32] Wätzel J, Sherman E Y and Berakdar J 2020 *Phys. Rev.* B **101** 235304
[33] Barrera R G, Estevez G A and Giraldo J 1985 *Eur. J. Phys.* **6** 287
[34] Baruffa F, Stano P and Fabian J 2010 *Phys. Rev.* B **82** 045311
[35] Bidégaray B 2003 *Numer. Methods PDE* **19** 284
[36] Wootters W K 1998 *Phys. Rev. Lett.* **80** 2245
[37] Sun Q-F and Xie X C 2005 *Phys. Rev.* B **72** 245305
[38] Stano P and Fabian J 2005 *Phys. Rev.* B **72** 155410
[39] Stano P and Fabian J 2006 *Phys. Rev. Lett.* **96** 186602
[40] Nitta J, Akazaki T, Takayanagi H and Enoki T 1997 *Phys. Rev. Lett.* **78** 1335
[41] Ganichev S D and Golub L E 2014 *Phys. Status Solidi* B **251** 1801
[42] Takeda J, Yoshioka K, Minami Y and Katayama I 2018 *J. Phys. D: Appl. Phys.* **51** 103001
[43] Hawrylak P 1993 *Solid State Commun.* **88** 475
[44] Simonin J, Proetto C R, Barticevic Z and Fuster G 2004 *Phys. Rev.* B **70** 205305
[45] Pons Viver M and Puente A 2019 *J. Math. Phys.* **60** 081905